Numerical simulations of axisymmetric inertial waves in a rotating sphere by finite elements

Jorge D'Elía ‡, Norberto Nigro ‡and Mario Storti ‡

‡Centro Internacional de Métodos Computacionales en Ingeniería (CIMEC)
Instituto de Desarrollo Tecnológico para la Industria Química (INTEC)
Universidad Nacional del Litoral - CONICET
Güemes 3450, 3000-Santa Fe, Argentina

e-mail: (jdelia, nnigro, mstorti)@intec.unl.edu.ar
web page: http://venus.ceride.gov.ar/cimec

Abstract

Axisymmetric inertial waves of a viscous fluid that fill a perturbed rotating spherical container are numerically simulated by finite elements. A laminar flow of an incompressible viscous fluid of Newtonian type is assumed in the numerical simulations. A monolithic computational code is employed, which is based on stabilized finite elements by means of a Streamline Upwind Petrov Galerkin (SUPG) and Pressure Stabilized Petrov Galerkin (PSPG) composed scheme. The Reynolds number is fixed as 50 000, while the ranges of the Rossby and Ekman numbers are $0.2 \leq \mathrm{Ro} \leq 1$ and $2 \times 10^{-5} \leq \mathrm{Ek} \leq 10^{-4}$, respectively. Some flow visualizations are performed. The pressure coefficient spectrum at the centre of the sphere is plotted as a function of the frequency ratio and some resonant frequencies are identified. The position of these resonant frequencies are in good agreement with previous experimental and analytical ones in the inviscid limit.

Key Words: rotating flows, axisymmetric inertial waves, finite elements, numerical methods, fluid mechanics

1 Introduction

As it is known, in the absence of rotation (or buoyancy due to a stable density stratification or magnetohydrodynamic effects), a fluid differs in an essential way from a solid in its inability to resist shearing stresses and, thereby, support shear waves. Thus, when a fluid rotates relative to an inertial frame the constraints imposed on the fluid system by the angular momentum conservation principle are such as to endowed the fluid with pseudo-elastic properties, the so-called "elastoid-inertial waves" or, more briefly, "inertial waves", e.g. see Hide[11]. These should not be confused with the "inertial waves" in the oceanographic literature, where this term is often used to designate rotationally modified internal gravity waves of frequencies slightly above or at the inertial frequency[14].

Thus, inertial waves in a fluid denotes those oscillatory motions of a rotating fluid that owe their existence neither to free surfaces nor to compressibility nor to any density stratification. It is a periodic disturbance fluid response motion (or normal mode) to a perturbation in a rotating flow of an incompressible fluid that is rotating almost rigidly in a container whenever the Coriolis forces are predominant. They are transverse waves (the perturbation velocity is perpendicular to the propagation direction), circularity polarized and dispersive. This is the only possible type of wave in an incompressible rotating fluid, e.g. see Shivamoggi[18]. In the laboratory experiments, a stationary observer sees these inertial waves in as an inward-outward faster-slower vortex. Inertial waves are also relevant in the understanding

of some wave phenomena in geophysics and planetary physics, e.g. recent identifications of inertial waves in the earth fluid core from superconducting gravimetric data created new interest in this classical problem. There appears growing recognition by the geophysical community that the inertial-wave observation may provide information about the physical and dynamical properties of the Earth interior, e.g. see Zhang[28].

The low-order modes with rather simple structure are more easily excited and may occur spontaneously even in situations not designed for them, e.g. a space vehicle with a liquid-filled tank that it is spinned-stabilized. These features are contradictory and can cause it to tumble out of control. For instance, the rotation of a top container may be unstable when the nutation and the sloshing are nearly resonant, since the nutation acts as a forcing for the sloshing which thus steadily excited[20]. If the container imparts some energy to the liquid, then reciprocally the liquid must exert a torque on the container. A remedy might well to be ascertain what sort of tanks avoids sloshing, e.g. see McIntyre-Tanner[15].

In order for the inertial waves to be generated the disturbance frequency (or disturbance spin) ω must be less than twice the stationary spin Ω, that is, $\omega < 2\Omega$. When this condition is met, the disturbing force is less than the restoring one supplied by the Coriolis acceleration and, in absence of viscous damping, the fluid will continue to oscillate. But, when $\omega > 2\Omega$ the restoring force will not to be large enough to balance the disturbing one, and the rigid-body rotation state is reached. As Henderson-Aldridge[1] remark, a global inertial wave belongs to a set of distinct eigenmodes with a discrete spectrum of eigenfrequencies, but not every shape of the cavity allows these in a fluid.

In the inviscid limit, the corresponding governing mathematical model is the Poincaré system, which has some unusual mathematical properties. A distinctive difficulty of the Poincaré system is that its eigenvalue λ_m appears both in the differential equation as at its boundary condition (e.g. see Appendix). Then, the mathematical problem is improperly-posed in the Hadamard sense (e.g. see Stewartson-Rickard[21]) but, under the assumption that the solutions are well-behaved, many properties can be found. Thus, the Poincaré equation can be elliptic when $|\lambda_m| > 2$ (so there is not inertial waves), parabolic when $|\lambda_m| = 2$, and hyperbolic when $|\lambda_m| < 2$, see Fig. 1. In the elliptic case the flow is continuous everywhere while only in the hyperbolic case there are inertial waves. In the last case, there exist real characteristic conical surfaces (similar to the Mach cone in gas dynamics), with a frequency dependent slope, across which the disturbances become discontinuous (e.g. the pressure becomes infinity) and dividing the flow into three separate regions, the inside one resemble the elliptic case while the adjustment from the inside the cone to the outside is made through thin viscous shear layers about the cone surface.

Although the general implicit forms of solutions for the Poincaré equation either in modified oblate spheroidal coordinates or in cylindrical coordinates (in which some roots of the associated Legendre function are involved in the summation of polynomials) have been available for a long time (e.g. Greenspan[6] review analytical expressions of eigenfrequencies and eigenmodes), separable solutions are restricted to geometries with axial symmetry, as cylinders (with or without an inner one) and axial spheroids (of which only the subclass of toroidal modes survives in a spherical shell), e.g. see Zhang[28]. Nevertheless, analytical methods are only adequate in the inviscid limit for few simple cases, and, consequently, recourse must be had to numerical methods for most general cases.

On the other hand, there are many precedents of computational models for inertial waves in several flow cases. Thus, Tan[24] *et al.* performs a time-dependent integral equation based in a linearized fluid flow formulation. Heuser[10] *et al.* performs a time-marching finite difference solution of the linearized axisymmetric flow equations on a right circular cylinder. Amberg-Ungarish[2] develop a finite difference solution for the spin-up from rest of a separating fluid-particle mixture in a cylindrical container, filled with a stationary mixture of initially uniform particle volume fraction, which is instantaneously set into rapid rotation. Moreover, there are also numerical models on the basis of variational principles. Thus, Aldridge[1] applied a classical Ritz method, whereas McIntyre-Tanner[15] and Henderson-Aldridge[9] used a finite-element method. In the last case, a variational principle for the inviscid limit (the Poincaré equation) is proposed, where the low-order frequencies are obtained as the roots of a secular equation.

Nevertheless, the Henderson-Aldridge[9] finite-element is specialized to inertial waves in the inviscid limit. Thus, the main aim of this work is to apply a more general finite element scheme for modelling inertial waves in the viscous case. In this work, numerical simulations are performed for the lowest inertial modes with axisymmetric symmetry that can be excited in a viscous fluid that fills a sphere when is rotating around its vertical axis with a prescribed unsteady spin speed. It is assumed a laminar regime with an incompressible fluid of Newtonian type. An identification of the low-order pressure resonances and flow visualization of the related flow patterns are also included. As validation of the present numerical simulations, they are compared with the corresponding ones to the inviscid limit and Aldridge-Toomre[1] experiments.

2 Physical formulation

2.1 The spin-up flow problem

In the spin-up flow problem, an impulsive change on the spin rate of the container leads boundary-layer induced accelerations and a pumping of the interior fluid is developed until a new dynamic equilibrium state is attained. For instance, Greenspan-Howard[7] and Veijst[8], give a careful analysis of the flow arising in closed rotating containers when the spin Ω is instantaneously increased with a small amount $\Delta\Omega > 0$. As a reaction to the increased spin $\Omega + \Delta\Omega$, Ekman layers develop at the container walls in which the flow is directed outwards along it (the *Ekman suction flow*). This outflow near the wall is compensated by a weak radial flow toward to the interior domain (outside the Ekman layers). This circulation in the meridional planes driven by the Ekman layers brings interior fluid from larger radii to smaller radii and provides the spin-up mechanism: in order to conserve its angular momentum, the fluid in a ring of decreasing radius acquires larger azimuth velocity. For instance, in Fig. 2 we have sketched a low order mode with axisymmetric symmetry that it can be excited in a rotating liquid sphere by a nonstationary spin, where (i) an inwardly moving spin-up front that separates the inner core I, with the old spin Ω and the partly spun-up region III, with the new value $\Omega + \Delta\Omega$; (ii) a quasi-steady very thin Ekman boundary layer near the walls, region II, that continuously extract fluid from region I and feed it into the spun-up region III. The nonstationary process is effectively completed when all fluid in region I has been flushed into region III.

2.2 Axisymmetric inertial oscillations of a rotating liquid sphere

The Aldridge-Toomre[1] work demonstrated the existence of axisymmetric spherical inertial waves. It is a detailed investigation based on experiments with a rigid fluid-filled spherical container whose spin about the vertical axis was forcibly varied in a smooth sinusoidal way about a non-null value, see Fig. 3. Their objectives were to excite, measure and compare with the theory in the inviscid limit, some of the inertial eigen modes within a low viscosity liquid, through the mild pumping of the thin viscous boundary layer near the sphere wall, where the energy input to the fluid system being represented by the term $\nu\nabla(\boldsymbol{u} \times \boldsymbol{\zeta})$, where ν is the kinematic viscosity of the fluid.

A polished transparent sphere of internal radius $R = 10$ cm, completely filled with water was fastened to a shaft that was in turn supported vertically by bearings mounted on a turntable. By means of a crank and torsion-bar dispositive the shaft and sphere together could be made to reciprocate relative to the turntable with an arbitrary half-amplitude ε (an expansion parameter) and a disturbance frequency ω. The turntable itself was driven coaxially with the shaft at a steady rate Ω, thereby imparting to the sphere the nonstationary spin $\tilde{\Omega}(t) = \Omega + \varepsilon\omega\cos(\omega t)$, where ε was fixed, so imposed changes in the ratio ω/Ω were made by altering the turntable speed in a continuous variable transmission.

The resonant inertial oscillations of the fluid in the sphere were made visible by introducing dye and suspended aluminum flakes. The experimental amplitude pressure measurements refer to the disturbance pressure differences

between the tip of a non-rotating hollow tube immersed along the axis to the sphere center and the free surface of the fluid at a 1.2 cm diameter hole drilled into its north pole. Only axisymmetric inertial oscillations which involve no motions across the equatorial plane are excited. The Ekman number is written as $\mathrm{Ek} = \nu/(\omega \mathrm{R}^2)$, where ν is the kinematic viscosity of the fluid, and the Rossby number is written as $\mathrm{Ro} = \omega/\Omega$ (omitting the expansion parameter ε), e.g. see Table 1.

As it is known in the theory of rotating fluids, all the directs effects of a slight kinematic viscosity ν on, at least, the low-order modes are confined to thin unsteady boundary layers so, when the fluid motion deep in the interior is one of the excited modes, the mean rate of energy dissipation is related to the free decay rate of a particular mode. On the other hand, the average energy rate transmitted to the fluid from its container by viscous surface stresses combined with unsteady motion is related both the free decay rate of a particular mode and the balance between the mean energy input and dissipation. In the numerical simulations a warning issue is related to the limit $\nu \to 0$ since all resonances become arbitrarily narrow, so there is a great complexity of the fluid response. The response spectrum consists of the pressure coefficient C_p measured between the pole and the center of the sphere for various frequency ratios Ω/ω whilst the container oscillated steadily with a half-amplitude $\varepsilon = 8^0$, where the turntable speed Ω and not the oscillation rate ω that is altered from one measurement to the next. The maximum pressure difference amplitudes $|\Delta p|$, between the pole and the sphere center $z = 0$ and between the pole and the point $z = R/2$ on the axis, are reported in terms of the dimensionless pressure coefficient $C_p = |\Delta p|/(\rho \varepsilon \omega^2 R^2)$.

Several distinct resonances were detected via pressure measurements made along the axis for various discrete ratios ω/Ω, of the spin excitation ω to the mean spin Ω. For the three most pronounced of these modes, the observed ratios ω/Ω were found to agree with the theory. These experiments and further works on spherical shells had emphasized some ill-posed problems in the theory of partial differential equations. As it is known in the theory of rotating flows, the inertial eigen-frequencies are found solving a hyperbolic differential equation with real characteristic under Dirichlet-Neumann boundary conditions (the Poincaré equation in the inviscid case).

3 Mathematical formulation

The Navier-Stokes equations for the motion of a viscous and incompressible fluid enclosed in a domain V and boundary S, see Fig. 4, can be written as

$$\nabla \cdot \boldsymbol{u} = 0 \; ; \tag{1}$$

$$\rho \left(\partial_t \boldsymbol{u} + \boldsymbol{u} \cdot \nabla \boldsymbol{u} \right) = \nabla \cdot \boldsymbol{\sigma} + \boldsymbol{f} \; ; \tag{2}$$

in $V \times [0, T]$. The position vector $\boldsymbol{x} = (x, y, z)$ is related to an Eulerian reference system, t is the time variable, V is the flow region, $[0, T]$ is some time interval, $\boldsymbol{f}$ is the volumetric source term while $\boldsymbol{u} = (u_x, u_y, u_z)$ and ρ are the velocity and density of the fluid, respectively. For a fluid with dynamic viscosity μ, the stress tensor $\boldsymbol{\sigma}$ can be decomposed into the isotropic and deviatoric parts, i.e. $\boldsymbol{\sigma} = -p\boldsymbol{I} + \boldsymbol{T}$, where p is the pressure, $\boldsymbol{I}$ is the identity matrix and $\boldsymbol{T} = 2\mu \boldsymbol{D}(\boldsymbol{u})$, where

$$\boldsymbol{D}(\boldsymbol{u}) = \frac{1}{2} \left[\nabla \boldsymbol{u} + (\nabla \boldsymbol{u})^T \right] \; . \tag{3}$$

Both the Dirichlet and Neumann boundary conditions are taken into account

$$\begin{aligned} \boldsymbol{u} &= \boldsymbol{g} \qquad \text{on } S_g; \\ \boldsymbol{n} \cdot \boldsymbol{\sigma} &= \boldsymbol{h} \qquad \text{on } S_h; \end{aligned} \tag{4}$$

where S_g and S_h are complementary subsets of the boundary S. The initial condition is a specified divergence-free velocity field $\boldsymbol{u}(\boldsymbol{x}, \boldsymbol{0}) = \boldsymbol{u}_0$ on the domain V.

4 Stabilized finite elements by a SUPG-PSPG alternative

The numerical simulations are performed by a stabilized finite element scheme for the unsteady Navier-Stokes Eqs. 1-2, where at each node and at every time step the moment and continuity equations are solved for the three components of velocity and pressure. For simplicity, equal order spatial discretization for pressure and velocity is highly attractive (i.e. linear tetrahedral elements), but it is well known that this kind of basis functions need to be stabilized to achieve stable solutions. The source of these instabilities is mainly the high Reynolds number that describes an advection dominated flow and the incompressibility constraint. The combined Streamline Upwind Petrov Galerkin (SUPG)[12,3] and Pressure Stabilizing Petrov Galerkin (PSPG) [25,26] scheme is employed for stabilization of the advection and incompressibility terms. Advection at high Reynolds numbers is stabilized with the SUPG operator, while the PSPG one stabilizes the incompressibility condition, which is responsible of the checkerboard pressure modes.

4.1 The SUPG-PSPG formulation

The incompressible Navier-Stokes equations present two important difficulties for the solution with finite elements. First, the character of these equations become highly advective dominant when the Reynolds number increases. In addition, the incompressibility condition represents not an evolution equation but a constraint on the equations. This has the drawback that only some combinations of interpolation spaces for velocity and pressure can be used with the Galerkin formulation, namely those that satisfy the so-called Ladyzhenskaya-Brezzi-Babuska condition. The advection and the incompressibility equations are stabilized with the SUPG and PSPG stabilization terms, respectively. In this way, it is possible to use stable equal order interpolations. To enforce the satisfaction of the discrete continuity equation an extra stabilization term is added, called LSIC (for Least Square Incompressibility Constraint). The flow domain Ω is partitioned in E finite elements Ω^e, with $e = 1, 2, \ldots, E$, while the interpolation spaces and weighting functions are defined as:

$$\begin{aligned} \mathcal{S}_{\boldsymbol{u}}^h &= \left\{ \boldsymbol{u}^h \mid \boldsymbol{u}^h \in H_d^h \text{ and } \boldsymbol{u}^h = \boldsymbol{g}^h \text{ on } \Gamma_g \right\} \\ \mathcal{S}_p^h = \mathcal{V}_p^h &= \left\{ q^h \mid q^h \in H_1^h \text{ with } \int_\Omega q^h d\Omega = 0 \text{ and } q^h\big|_{\Gamma_h} = 0 \right\} \\ \mathcal{V}_{\boldsymbol{u}}^h &= \left\{ \boldsymbol{w}^h \mid \boldsymbol{w}^h \in H_d^h \text{ and } \boldsymbol{w}^h = \mathbf{o} \text{ on } \Gamma_g \right\} \end{aligned} \tag{5}$$

with $H_d^h = \left(H_1^h\right)^d$, where d is the number of space dimensions and the Sobolev space

$$H_1^h = \left\{ \phi^h \text{ such that } \phi^h \in C^0(\overline{\Omega}) \text{ and } \phi^h|_{\Omega^e} \in \mathcal{L}^1 \right\} \ ; \tag{6}$$

for all $\Omega^e \in \mathcal{E}$, where $\mathcal{L}^1$ is the set of polynomials of first order while $\mathcal{E}$ is the set of elements. The combined SUPG[12,3] and PSPG[25,26,27] formulation for Eqs. (1-2) can be written as: find $\boldsymbol{u}^h \in \mathcal{S}_{\boldsymbol{u}}^h$ and $p^h \in \mathcal{S}_p^h$ such that:

$$\begin{aligned} &\int_\Omega \boldsymbol{w}^h \cdot \rho\Big(\partial_t \boldsymbol{u}^h + \boldsymbol{u}^h \cdot \nabla \boldsymbol{u}^h\Big) d\Omega + \int_\Omega \boldsymbol{D}(\boldsymbol{w}^h) : \boldsymbol{\sigma}^h d\Omega \ + \\ &+ \underbrace{\sum_{e=1}^{E} \int_{\Omega^e} \boldsymbol{\delta}^h \cdot \Big[\rho\left(\partial_t \boldsymbol{u}^h + \boldsymbol{u}^h \cdot \nabla \boldsymbol{u}^h\right) - \nabla \cdot \boldsymbol{\sigma}^h\Big] d\Omega}_{\text{(SUPG)}} \ + \\ &+ \underbrace{\sum_{e=1}^{E} \int_{\Omega^e} \boldsymbol{\epsilon}^h \cdot \Big[\rho(\partial_t \boldsymbol{u}^h + \boldsymbol{u}^h \cdot \nabla \boldsymbol{u}^h) - \nabla \cdot \boldsymbol{\sigma}^h\Big] d\Omega}_{\text{(PSPG)}} \ + \\ &+ \sum_{e=1}^{E} \int_{\Omega^e} \nu_{\text{LSIC}} \nabla \cdot \boldsymbol{w}^h \nabla \rho \cdot \boldsymbol{u}^h d\Omega + \int_\Omega q^h \nabla \cdot \boldsymbol{u}^h d\Omega = 0 \ ; \end{aligned} \tag{7}$$

for all $\boldsymbol{w}^h \in \mathcal{V}_{\boldsymbol{u}}^h$ and $q^h \in \mathcal{V}_p^h$. In Eq. (7) three additional stabilization terms are added to the standard Galerkin formulation: the parameter $\boldsymbol{\delta}^h$ corresponds to the SUPG stabilization, the $\boldsymbol{\epsilon}^h$ parameter corresponds to the PSPG one, and finally the ν_{LSIC} parameter to enforce the incompressibility contraint. The first two terms are defined over different functional spaces and they can be written as $\boldsymbol{\delta}^h = \tau_{\text{SUPG}}\ (\boldsymbol{u}^h \cdot \nabla)\boldsymbol{w}^h$ and $\boldsymbol{\epsilon}^h = \tau_{\text{PSPG}}\ \rho^{-1}\nabla q^h$, where

$$\begin{aligned} \tau_{\text{SUPG}} &= \frac{h_{\text{e}}}{2||\boldsymbol{u}^h||}\ z(\text{Re}_{\text{u}^\text{h}})\ ; \\ \tau_{\text{PSPG}} &= \frac{h_{\text{e}}^*}{2||\boldsymbol{U}||}\ z(\text{Re}_{\text{U}}^*)\ ; \\ \nu_{\text{LSIC}} &= \frac{h_{\text{e}}^*}{2}||\boldsymbol{u}^h||\ z(\text{Re}_{\text{u}^\text{h}})\ ; \end{aligned} \tag{8}$$

while $\text{Re}_{\text{u}^\text{h}}$ and Re_{U}^* are the Reynolds number based on the element velocity $\boldsymbol{u}^h$ and a global characteristic velocity $\boldsymbol{U}$, respectively, that is,

$$\text{Re}_{\text{u}^\text{h}} = \frac{||\boldsymbol{u}^\text{h}||\ \text{h}_\text{e}}{2\nu} \quad \text{and} \quad \text{Re}_{\text{U}}^* = \frac{||\boldsymbol{U}||\ \text{h}_\text{e}^*}{2\nu}\ . \tag{9}$$

The element size h_e is computed as

$$h_\text{e} = 2\left[\sum_{a=1}^{n_e} |\boldsymbol{s}\cdot\nabla w_a|\right]^{-1}\ ; \tag{10}$$

where w_a is the function associated to node a, n_e is the number of nodes connected to the element and $\boldsymbol{s}$ is the streamline oriented unit vector, while the element size h_e^* is defined as the diameter of the sphere with the same element volume. Finally, the function $z(\text{Re})$ in Eqs. (8) is defined as

$$z(\text{Re}) = \begin{cases} \text{Re}/3 & 0 \le \text{Re} < 3\ ; \\ 1 & 3 \le \text{Re}\ . \end{cases} \tag{11}$$

4.2 Spatial discretization

Spatial discretization leads to the following equation system (e.g. see[26, 25])

$$(\boldsymbol{M}+\boldsymbol{M}_\delta)\boldsymbol{a} + \boldsymbol{N}(\boldsymbol{v}) + \boldsymbol{N}_\delta(\boldsymbol{v}) + (\boldsymbol{K}+\boldsymbol{K}_\delta)\boldsymbol{v} - (\boldsymbol{G}-\boldsymbol{G}_\delta)\boldsymbol{p} = \boldsymbol{F}+\boldsymbol{F}_\delta\ ; \tag{12}$$

$$\boldsymbol{G}^T\boldsymbol{v} + \boldsymbol{M}_\epsilon\boldsymbol{a} + \boldsymbol{N}_\epsilon(\boldsymbol{v}) + \boldsymbol{K}_\epsilon\boldsymbol{v} + \boldsymbol{G}_\epsilon\boldsymbol{p} = \boldsymbol{E}+\boldsymbol{E}_\epsilon\ ; \tag{13}$$

where

$$\boldsymbol{v} = \text{Array}\left\{\boldsymbol{u}^h\right\}\ ; \tag{14}$$

$$\boldsymbol{a} = \dot{\boldsymbol{v}}\ ; \tag{15}$$

$$\boldsymbol{p} = \text{Array}\left\{p^h\right\}\ ; \tag{16}$$

are the nodal vectors of velocities, accelerations and pressures, respectively. The mass matrices are obtained from the time-dependent terms and are given by

$$\boldsymbol{M} = \int_V \boldsymbol{w}^h\rho\boldsymbol{w}^h dV\ ; \tag{17}$$

$$\boldsymbol{M}_\delta = \int_V \boldsymbol{\delta}^h\rho\boldsymbol{w}^h dV\ ; \tag{18}$$

$$\boldsymbol{M}_{\boldsymbol{\epsilon}} = \int_V \boldsymbol{\epsilon}^h\rho\boldsymbol{w}^h dV\ ; \tag{19}$$

while the stiffness ones are obtained from the viscous terms and are given by

$$\boldsymbol{K} = \int_V \frac{\mu}{2}[\nabla \boldsymbol{w}^h + \nabla(\boldsymbol{w}^h)^T] : [\nabla \boldsymbol{w}^h + \nabla(\boldsymbol{w}^h)^T] \; dV \; ; \tag{20}$$

$$\boldsymbol{K}_\delta = -\int_V \boldsymbol{\delta}^h \cdot \nabla \cdot [2\mu \boldsymbol{D}(\boldsymbol{w}^h)] \; dV \; ; \tag{21}$$

$$\boldsymbol{K}_\epsilon = -\int_V \boldsymbol{\epsilon}^h \cdot \nabla \cdot [2\mu \boldsymbol{D}(\boldsymbol{w}^h)] \; dV \; . \tag{22}$$

The $\boldsymbol{G}$ matrices are obtained from the pressure terms and are given by

$$\boldsymbol{G} = \int_V q^h \nabla \cdot \boldsymbol{w}^h dV \; ; \tag{23}$$

$$\boldsymbol{G}_\delta = \int_V \boldsymbol{\delta}^h \cdot \nabla q^h dV \; ; \tag{24}$$

$$\boldsymbol{G}_\epsilon = \int_V \boldsymbol{\epsilon}^h \cdot \nabla q^h dV \; ; \tag{25}$$

and, finally, the $\boldsymbol{N}$ matrices are obtained from the advective terms and are given by

$$\boldsymbol{N} = \int_V \boldsymbol{w}^h \cdot \rho \boldsymbol{u}^h \cdot \nabla \boldsymbol{u}^h dV \; ; \tag{26}$$

$$\boldsymbol{N}_\delta = \int_V \boldsymbol{\delta}^h \cdot \rho \boldsymbol{u}^h \cdot \nabla \boldsymbol{u}^h dV \; ; \tag{27}$$

$$\boldsymbol{N}_\epsilon = \int_V \boldsymbol{\epsilon}^h \cdot \rho \boldsymbol{u}^h \cdot \nabla \boldsymbol{u}^h dV \; . \tag{28}$$

The vector $\boldsymbol{F}$ arises from the imposition of both Dirichlet and Neumann boundary conditions while the vector $\boldsymbol{E}$ arises only from the Dirichlet ones.

4.3 SUPG-PSPG finite element solver

The SUPG-PSPG finite element alternative is implemented by the PETSc-FEM[19] code, which is a parallel multi-physics finite element library based on the Message Passing Interface (MPI, http://www.mpi-forum.org) and the Portable Extensible Toolkit for Scientific Computations (PETSc, http://www-fp.mcs.anl.gov/petsc). Among CFD applications of this flow-solver include, for instance, hydrology[16], free surface flows[5,4] and added mass computations[23].

5 Numerical experiments

5.1 Geometrical, fluid and flow parameters

The flow properties and kinematic data used in the present numerical experiments are chosen taking into account, on one hand, that each test-run is computed with a time marching procedure, which is an high CPU-time consuming task and, on the other hand, previous experimental or semi-analytical related works in the inviscid limit ($\nu \to 0$) as those performed by Kudlick,[13] Greenspan[6] and Aldridge-Toomre[1].

In the numerical simulations, a sphere of radius $R = 1$ [m] is considered, see Fig. 4. The sphere is filled with an incompressible and viscous fluid of Newtonian type, unitary fluid density $\rho = 1$ [kg/m^3] and kinematic viscosity ν (later defined). The sphere performs an unsteady spin motion around its vertical axis given by

$$\hat{\Omega}\ (t;\omega) = \Omega + \varepsilon\omega \cos(\omega t) \; ; \tag{29}$$

with the steady spin $\Omega = 1$ [rad/s], the expansion parameter $\varepsilon = 8^o$, while t is the time (independent variable) and ω is the disturbance spin as a free parameter. As the steady spin Ω is fixed, the disturbance frequency interval is $0.2 \leq \omega \leq 1$. The expression given by Eq. 29 and remaining values are taken following the Aldridge-Toomre[1] work.

A laminar regime with a Reynolds number Re = 50 000 is chosen. Then, the kinematic viscosity is computed as $\nu = \Omega R^2/\mathrm{Re}$. Then, the corresponding Rossby and Ekman number intervals are obtained by means of definitions given in Table 1 and resulting values are shown in Table 2.

5.2 Finite element mesh

An axisymmetric finite element mesh is employed which has 4.3 K-hexaedra and 8.9 K-nodes. This is a two-dimensional (2D) mesh for a radial-vertical $r-z$ plane (or meridional plane) with one element row in the circumferential direction. Fig. 5 shows a vertical view of the obtained grid, where mesh refinement is performed near the sphere walls since the physics phenomena is mostly governed by the boundary layer formed by the wall movement and the inertial fluid, that is, the mild pumping action of the unsteady (and very thin) Ekman boundary layer.

5.3 Boundary conditions and time step

The tests are performed on an inertial system of reference, i.e. where the observer is at rest. Therefore, the boundary conditions are those of the rigid-body rotation, with nonstationary speed on the sphere walls. In order to avoid the rigid pressure modes, a reference pressure value is imposed on an arbitrary node, for instance, on the sphere center.

In order to perform a plot of the pressure coefficient as a function of the frequency ratio Ω/ω, a number of $N_T = 28$ test-runs are performed in the frequency-ratio interval $1 \leq \Omega/\omega \leq 5$. The time step Δt is selected in such way that there are $n = 32$ points per perturbation period in each run. They are variable according to the perturbation spin ω and given by $\Delta t = (2\pi/(n\omega)$, with a total of about $N_T = 5$ periods, approximately.

5.4 Semi-analytical solution in the inviscid limit

In the inviscid limit a semi-analytical solution can be performed. In this case, the theory of Stewartson-Roberts[22] is applicable for spheroidal containers, where separable solutions are possible in oblate spheroidal coordinates chosen to transform the Poincaré equation from the (x,y,z) coordinates to $(x,y,iz/\lambda)$ ones, where $i = \sqrt{-1}$. The cylindrical (s,ϕ,z) coordinates are written into the oblate spheroidal (η,μ,ϕ) ones as

$$\begin{cases} s = (4\alpha^2 - \eta^2)^{1/2}(1-\mu^2)^{1/2} \ ; \\ z = (\beta^2 - 1)^{1/2}\eta\mu \ ; \end{cases} \tag{30}$$

where $|\mu| \leq 1$ and

$$\alpha^2 = \frac{1}{4-\lambda^2} \quad ; \quad \beta^2 = \frac{4}{\lambda^2} \ ; \tag{31}$$

The unit sphere equation in these coordinates is transformed with

$$s^2 + z^2 - 1 = (\alpha^2\lambda^2 - \eta^2)(1 - \beta^2\mu^2) = 0 \ ; \tag{32}$$

which is reduced to

$$\eta = \alpha\lambda = \frac{\lambda}{\sqrt{4-\lambda^2}} \ ; \tag{33}$$

and the modal pressure, solution of Eq. 48, can be separated as

$$P_{k,m}(\eta,\mu,\phi) = L_{k,m}(\gamma\eta)\ L_{k,m}(\mu)\ e^{im\phi} \ ; \tag{34}$$

where $k = 1, 2, ...$ and $m = 1, 2, .., k$, with $\gamma = 1/(2\alpha)$ while $L_{k,m}$ is the m-associated Legendre polynomial of k-order. In the Aldridge-Toomre[1] laboratory experiment, only axisymmetric inertial oscillations which involve no motions across the equatorial plane are excited. Nevertheless, the number of inviscid inertial modes is denumerable infinite and its resonant non-dimensional eigenfrequencies are predicted to be

$$\frac{\Omega}{\omega_{n,m}} = \frac{1}{2x_{n,m}} \; ; \tag{35}$$

where $x_{n,m}$ is the mth of the n zeros of the first associated Legendre polynomial $L_{2n+2,1}$ of $2n+2$ order, in the interval $0 < x < 1$. In Table 3 some of the non-dimensional eigenfrequencies $\Omega/\omega_{n,m}$ of the axisymmetric inertial (n, m) cell-modes predicted by Eq. 35 are listed according to this inviscid theory.

5.5 Detected pressure resonances and flow patterns

Returning to the viscous case, the numerical simulations allow to detect pressure resonances and to plot the related flow patterns. For the pressure increments, the maximum pressure difference amplitude $|\Delta p|$ (between the upper pole and the sphere center) is found for each test-run, and then is expressed in terms of the dimensionless pressure coefficient $C_p = |\Delta p|/\gamma$, where $\gamma = (\rho\varepsilon\omega^2 R^2)$. Thus, the response spectrum consists of the pressure coefficient C_p plotted as a function of the frequency ratio Ω/ω, and it is shown in Fig. 6. From this figure, it is found that $N_p = 4$ resonance peaks are clearly identified. The corresponding flow-patterns at each pressure-peak are shown in Figs. 7-10.

The discrete frequency ratios ω_k/Ω of the four pressure peaks identified in Fig. 6 are found to agree with the theoretical ones in the inviscid limit $\nu \to 0$ that were obtained in Sec. 5.4 and summarized in Table 3. They are also to agree with the ones obtained by Greenspan[6] (Table 2.1 and Fig. 2.8, pp. 66-67) and shown in Table 4, as well the experimental ones reported by Aldridge-Toomre[1].

The numerical simulated flow-patterns at each pressure-peak for the viscous case are compared with the analytic ones in the inviscid limit $\nu \to 0$ that are sketched in Fig. 11 (taken from Fig. 2.7, p. 65, Greenspan[6]). It can be observed that:

- Pressure-peak 1 ($\Omega/\omega \approx 0.7640$): there is a dominant cell that corresponds, in the inviscid limit $\nu \to 0$, to the $(1, 1)$ cell-mode or fundamental one. See numerical simulation in Fig. 7 and analytical sketch in Fig. 11 (top-left);
- Pressure-peak 2 ($\Omega/\omega \approx 1.0660$): there are two dominant cells that correspond, in the inviscid limit $\nu \to 0$, to the $(2, 1)$ cell-mode. See numerical simulation in Fig. 8 and analytical sketch in Fig. 11 (top-right);
- Pressure-peak 3 ($\Omega/\omega \approx 1.3770$): there are three dominant cells that correspond, in the inviscid limit $\nu \to 0$, to the $(3, 1)$ cell-mode. See numerical simulation in Fig. 9 and analytical sketch in Fig. 11 (bottom-left);
- Pressure-peak 4 ($\Omega/\omega \approx 1.6910$): there are four dominant cells that correspond, in the inviscid limit $\nu \to 0$, to the $(4, 1)$ cell-mode. See numerical simulation in Fig. 10 and analytical sketch in Fig. 11 (bottom-right).

There are some other small cells that appears due to velocity inversion but these soon dissipate and they do not appear in these figures.

6 Discussion and conclusions

The theoretical eigenmodes in the inviscid limit $\nu \to 0$ sketched in Fig. 11 (taken from Fig. 2.7, p. 65, Greenspan[6]) are equatorially-symmetric placed. They are identified with integers (n, m), where n is the number of modes in a family and m is the number of cells along the vertical z-axis. These indicate how is the order of complexity in the

structure of an eigenmode. The eigenmodes by nature are distinctively organized into various eigencells. For all the cases considered, the eigencells are axisymmetric. Although the numerical simulations were made assuming a laminar flow with a Reynolds number of 50 000, the positions of the first four resonant frequencies with axisymmetric symmetry are close enough to the corresponding ones of the inviscid limit $\nu \to 0$, as well as the flow patterns show one cell for the first resonant frequency, two cells for the second one and so until the fourth one in consonance with the analytical inviscid inertial modes that were taken into in account in Sec. 5.5.

The four resonant frequencies distinctly revealed in the present numerical simulations are well compared with the experiment data of Aldridge-Toomre[1]. The coincidence between laboratory and numerical experiments in that bandwidth shows they are compatible since both have a low-order bias, that is, whether a study is experimental or numerical, the eigenmodes with the simplest structure are the easiest to excite or recover. On the other hand, perhaps it is more convenient to locate the related eigenmodes with a coarser mesh and then track them through some refinements and thus a better resolution of the eigencells can be obtained.

The overall approach is only limited by the restrictions of the assumed flow model (an unsteady laminar regime in a viscous and incompressible fluid of Newtonian type). The present numerical results support the conclusion that the standard SUPG-PSPG finite element method performed very well in the simulation of unsteady axisymmetric inertial waves of viscous fluids although the inviscid limit, the Poincaré equation, is improperly-posed in the Hadamard sense. On the other hand, the present approach allows consider other container geometries whose analytical or semi-analytical solutions cannot easily found. Future modeling efforts would be focused on a study of other items as truncation errors, grid independence and iterative convergence.

7 Acknowledgment

This work was performed with the *Free Software Foundation/GNU-Project* as `GNU/Linux OS` and `GNU/Octave`, as well another Open Source resources as `PETSc`, `MPICH` and `OpenDX`, and it was supported through grants CONICET PIP 02552/2000, ANPCyT FONCyT PME 209 Cluster, ANPCyT FONCyT PID 99-74 Flags, ANPCyT PICT 6973 BID 1201/OC-AR Proa and CAI+D-UNL 2000 43.

References

[1] K.D. Aldridge and A. Toomre. Axisymmetric inertial oscillations of a fluid in a rotating spherical container. *J. Fluid Mech.*, 37:307–323, 1969.

[2] G. Amberg and M. Ungarish. Spin-up from rest of a mixture: numerical simulation and asymptotic theory. *J. Fluid Mech.*, 246:443–464, 1993.

[3] A.N. Brooks and T.J.R. Hughes. Streamline upwind/Petrov-Galerkin formulations for convection dominated flows with particular emphasis on the incompressible Navier-Stokes equations. *Comp. Meth. App. Mech. Engng.*, 32:199–259, 1982.

[4] J. D'Elía, M.A. Storti, and S.R. Idelsohn. A panel-Fourier method for free surface methods. *ASME-J. of Fluids Engng.*, 122(2):309–317, June 2000.

[5] J. D'Elía, M.A. Storti, E. Oñate, and S.R. Idelsohn. A nonlinear panel method in the time domain for seakeeping flow problems. *Int. J. of Computational Fluid Dynamics*, 16(4):263–275, 2002.

[6] H.P. Greenspan. *The theory of rotating flows.* Cambridge University Press, 1968.

[7] H.P. Greenspan and L.N. Howard. On the time-dependent motion of a rotating fluid. *J. Fluid Mech.*, 17:385–404, 1963.

[8] G.J.F. Heijst. Spin-up phenomena in non-axisymmetric containers. *J. Fluid Mech.*, 206:171–191, 1989.

[9] G.A. Henderson and K.D. Aldridge. A finite-element method for inertial waves in a frustum. *J. Fluid Mech.*, 234:317–327, 1992.

[10] G.E. Heuser, R.J. Ribando, and H.G. Wood. A numerical simulation of inertial waves in a rotating fluid. *Computer Methods in Applied Mechanics and Engineering*, 57:207–222, 1986.

[11] R. Hide. The dynamics of rotating fluids. In P.H. Roberts and A.M. Soward, editors, *Rotating Fluids in Geophysics*, chapter 1, pages 1–28. Academic Press, London, 1978.

[12] T.J.R. Hughes and A.N. Brooks. A multi-dimensional upwind scheme with no crosswind diffusion. In ASME, editor, *Finite Element Methods for Convection Dominated Flows*, volume 34, pages 19–35. AMD, New York, 1979.

[13] M.D. Kudlick. *On transient motions in a contained rotating fluid*. PhD thesis, Massachusetts Institute of Technology, 1966.

[14] L.R.M. Maas. On the amphidromic structure of inertial waves in a rectangular parallelepiped. *Fluid Dynamics Research*, 33:373401, 2003.

[15] J.E. McIntyre and T.M. Tanner. Fuel slosh in a spinning ob-axis propellent tank: an eigenmode approach. *Space Commun. Broad.*, 5:229–251, 1987.

[16] R.R. Paz and M.A. Storti. An interface strip precondition for domain decomposition methods. application to hidrology. *Int. J. for Num. Meth. in Engng.*, 62(13):1873–1894, 2005.

[17] P.H. Roberts and A.M. Soward, editors. *Rotating Fluids in Geophysics*. Academic Press, London, 1978.

[18] B.K. Shivamoggi. *Theoretical Fluid Dynamics*. Wiley Inter-Science, USA and Canada, 1998.

[19] V.E. Sonzogni, A. Yommi, N.M. Nigro, and M.A. Storti. A parallel finite element program on a Beowulf Cluster. *Advances in Engineering Software*, 33:427–443, 2002.

[20] K. Stewartson. Homogeneous fluids in rotation: waves. In P.H. Roberts and A.M. Soward, editors, *Rotating Fluids in Geophysics*, chapter 1, pages 67–138. Academic Press, London, 1978.

[21] K. Stewartson and J.A. Rickard. Pathological oscillations of a rotating luid. *J. Fluid Mech.*, 35:759–773, 1969.

[22] K. Stewartson and P.H. Roberts. On the motion of a liquid in a spheroidal cavity of a precessing rigid body. *J. Fluid Mech.*, 17:1–20, 1963.

[23] M.A. Storti and J. D'Elía. Added mass of an oscillating hemisphere at very-low and very-high frequencies. *ASME-J. of Fluids Engng.*, 126(6):1048–1053, November 2005.

[24] D.G.H. Tan, M.E. McIntyre, and J.C. Jackson. Destabilization of spinning, nutating containers by an inviscid fluid flow: a time-dependent integral equation formulation. *J. Fluid Mech.*, 11:1–21, 1996.

[25] T.E. Tezduyar. Stabilized finite element formulations for incompressible flow computations. *Advances in Applied Mechanics*, 28:1–44, 1992.

[26] T.E. Tezduyar, S. Mittal, S. Ray, and R. Shih. Incompressible flow computations with stabilized bilinear and linear equal order interpolation velocity-pressure elements. *Comp. Meth. App. Mech. Engng.*, 95:221–242, 1992.

[27] T.E. Tezduyar and Y. Osawa. Finite element stabilization parameters computed from element matrices and vectors. *Comp. Meth. App. Mech. Engng.*, 190:411–430, 2000.

[28] K. Zhang. On equatorially trapped boundary inertial waves. *J. Fluid Mech.*, 248:203–217, 1993.

8 Appendix

In the following Sections 8.1 and 8.2, the inviscid inertial eigenmodes are considered, but they are only relevant as a reference for validate the corresponding ones of the viscous case that are predicted in the numerical simulations, and they are not taken into account in the numerical discretization by finite elements performed in Sec. 4.

8.1 Inertial eigenmodes for a rotating fluid

As it is known, the Coriolis and viscous forces play a dominant role in a fast rotating container filled with a viscous fluid, and they can measured by the Rossby and Ekman numbers, Ro and Ek, respectively (e.g. see Table 1). When the container moves at constant spin $\boldsymbol{\Omega}$ around its vertical axis z, the non-dimensional differential equations on the body axis can be written as (e.g. see Greenspan[6])

$$\partial_t \tilde{\boldsymbol{u}} + \mathrm{Ro}\ (\tilde{\boldsymbol{u}} \cdot \nabla)\tilde{\boldsymbol{u}} + 2\hat{\boldsymbol{z}} \times \tilde{\boldsymbol{u}} + \nabla \tilde{\mathrm{p}} = \mathrm{Ek}\ \nabla^2 \tilde{\boldsymbol{u}} \quad ; \quad \nabla \cdot \tilde{\boldsymbol{u}} = 0\ ; \tag{36}$$

where $\hat{\boldsymbol{z}}$ is the vertical unit vector, $\tilde{p}(\tilde{\boldsymbol{r}}, \tilde{t})$ is the nodimensional reduced pressure, $\times$ denotes vectorial product and ∇^2 is the Laplacian. The boundary and initial conditions include the no-slip condition $\tilde{\boldsymbol{u}} = \mathbf{o}$ at the solid walls S and some initial velocity $\tilde{\boldsymbol{u}}(\tilde{\boldsymbol{r}}, 0) = \tilde{\boldsymbol{u}}_0(\tilde{\boldsymbol{r}})$ which slightly differs from the rigid body rotation. Also the mass balance and no-slip boundary condition must be verified by the initial velocity $\tilde{\boldsymbol{u}}_0(\tilde{\boldsymbol{r}})$. Linearized equations for rotating flows implie a null Rossby number ($\mathrm{Ro} = 0$) and Eq. 36 reduces to

$$\partial_t \tilde{\boldsymbol{u}} + 2\hat{\boldsymbol{z}} \times \tilde{\boldsymbol{u}} + \nabla \tilde{p} = \mathrm{Ek} \nabla^2 \tilde{\boldsymbol{u}} \quad ; \quad \nabla \cdot \tilde{\boldsymbol{u}} = 0\ . \tag{37}$$

Thus, linearized equations of motion for a rotating flow (when $\mathrm{Ro} = 0$) either of a viscous fluid ($\mathrm{Ek} \neq 0$) or an inviscid one ($\mathrm{Ek} = 0$) admit separable solutions, i.e. the velocity and the pressure can be represented as a superposition of the inertial eigenmodes (e.g. see Greenspan[6], Roberts-Soward[17])

$$\begin{aligned} \tilde{\boldsymbol{u}} &= \sum_m \boldsymbol{U}^m e^{i\lambda_m \tilde{t}}; \\ \tilde{p} &= \sum_m P^m e^{i\lambda_m \tilde{t}}; \end{aligned} \tag{38}$$

where (U_m, P_m) is the m-inertial mode, velocity and pressure, respectively, λ_m is the m-eigenvalue and $i = \sqrt{-1}$ is the imaginary unity. For the inviscid case the eigenvalue λ_m is real, while for the viscous one is complex. In the last case, its imaginary part is a measure of the rate of the decay on the velocity due to viscous effects which are, in turn, confined to a thin boundary layer at the container wall of thickness $O(\sqrt{\mathrm{Ek}})$. On the other hand, until the diffusion has had sufficient time to thicken this boundary layer, a boundary layer analysis is also possible.

8.2 The inviscid case. The Poincaré equation

When rotational inertia dominates over viscosity and nonlinearity, thereby damping and interaction between modes are negligible, the spatial component of the inertial pressure modes P_m given in Eq. 38 are governed by the Poincaré

equation. Introducing Eq. 38 and the boundary conditions into Eq. 37, results in the frequency domain (Kudlick[13])

$$\begin{cases} i\lambda_m \boldsymbol{U}^m + 2\hat{\boldsymbol{z}} \times \boldsymbol{U}^m + \boldsymbol{F}^m = \mathbf{o} & \text{in } V; \\ \nabla \cdot \boldsymbol{U}^m = 0 & \text{in } V; \\ \boldsymbol{n} \cdot \boldsymbol{U}^m = 0 & \text{at } S; \end{cases} \tag{39}$$

for each m-inviscid mode, where $\boldsymbol{F}^m \equiv \nabla P^m$ is the pressure gradient and $\boldsymbol{n}$ is the surface normal unit. These equations represent the balance of momentum, fluid incompressibility and the slip boundary condition at the solid surfaces, respectively. The Cartesian components of the first Eq. 39 are

$$\left.\begin{aligned} i\lambda_m U_x^m - 2U_y^m &= -F_x^m \\ i\lambda_m U_y^m + 2U_x^m &= -F_y^m \\ i\lambda_m U_z^m &= -F_z^m \end{aligned}\right\} \tag{40}$$

The system determinant of Eq. 40 is $D = i\lambda_m(4-\lambda_m^2)$, which is regular whenever $|\lambda_m| \neq 2$. Solving by determinants

$$\begin{cases} U_x^m = \alpha \left[F_x^m - (2i/\lambda_m)\ F_y^m\right] \ ; \\ U_y^m = \alpha \left[F_y^m + (2i/\lambda_m)\ F_x^m\right] \ ; \\ U_z^m = \alpha \left[F_z^m - (4/\lambda_m^2)\ F_z^m\right] \ ; \end{cases} \tag{41}$$

where $\alpha = -i\lambda_m/(4-\lambda_m^2)$. As

$$\frac{-2}{i\lambda_m}\left(\boldsymbol{z} \times \boldsymbol{F}^m\right) = \frac{-2}{i\lambda_m}\begin{bmatrix} F_y^m \\ -F_x^m \\ 0 \end{bmatrix} \ ; \tag{42}$$

then, Eq. 41 can be written in the vectorial form

$$\boldsymbol{U}^m = \frac{-i\lambda_m}{4-\lambda_m^2}\left[\nabla P^m - \frac{2}{i\lambda_m}\left(\hat{\boldsymbol{z}} \times \nabla P^m\right) - \frac{4}{\lambda_m^2}\left(\hat{\boldsymbol{z}} \cdot \nabla P^m\right)\hat{\boldsymbol{z}}\right] . \tag{43}$$

Introducing the Cartesian components given by Eq. 41 into the differential mass balance equation of an incompressible fluid $\partial_x U_x + \partial_y U_y + \partial_z U_z = 0$, results

$$\partial_x U_x^m = \frac{-i\lambda_m}{4-\lambda_m^2}\left(\partial_x F_x^m - \frac{2}{i\lambda_m}\partial_x F_y^m\right) \ ; \tag{44}$$

$$\partial_y U_y^m = \frac{-i\lambda_m}{4-\lambda_m^2}\left(\partial_y F_y^m + \frac{2}{i\lambda_m}\partial_y F_x^m\right) \ ; \tag{45}$$

$$\partial_z U_z^m = \frac{-i\lambda_m}{4-\lambda_m^2}\left(\partial_z F_z^m - \frac{4}{\lambda_m^2}\partial_z F_z^m\right) \ ; \tag{46}$$

but $(F_x^m, F_y^m, F_z^m) = (P_{,x}^m, P_{,y}^m, P_{,z}^m)$, replacing and adding gives

$$\frac{-i\lambda_m}{4-\lambda_m^2}\left(P_{,xx}^m + P_{,yy}^m + P_{,zz}^m - \frac{4}{\lambda_m^2}P_{,zz}^m\right) = 0 \ ; \tag{47}$$

Introducing Eq. 43 in the slip boundary condition $\boldsymbol{n} \cdot \boldsymbol{U} = 0$, and from Eq. 47, resulting the Poincaré system

$$\begin{aligned} \nabla^2 P^m - \frac{4}{\lambda_m^2}\left(\hat{\boldsymbol{z}} \cdot \nabla\right)^2 P^m = 0 \qquad & \text{in } V; \\ \boldsymbol{n} \cdot \left[\nabla P^m - \frac{2}{i\lambda_m}\left(\hat{\boldsymbol{z}} \times \nabla P^m\right) - \frac{4}{\lambda_m^2}\left(\hat{\boldsymbol{z}} \cdot \nabla P^m\right)\hat{\boldsymbol{z}}\right] = 0 \qquad & \text{at } S. \end{aligned} \tag{48}$$

On the other hand, from momentum conservation principles, it can be shown that the eigenvalues λ_m are reals and that $|\lambda_m| < 2$ (e.g. see Kudlick[13]).

List of Figures

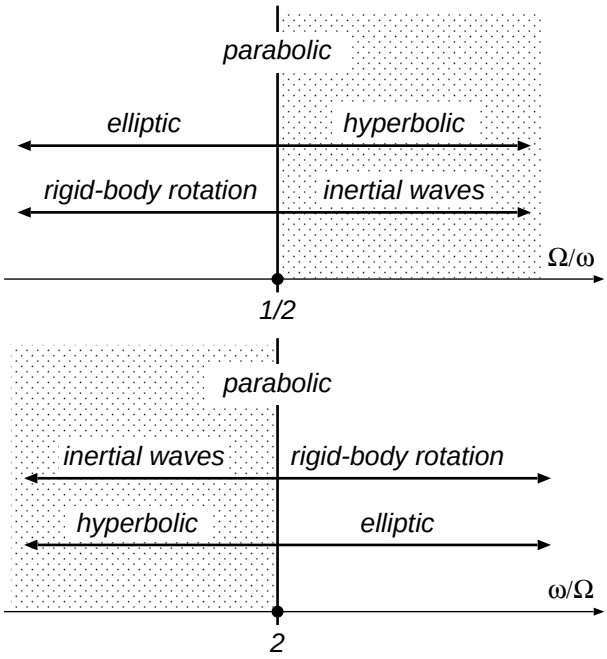

Figure 1: Type change of the Poincaré equation for the inviscid case, as a function of the frequency ratio Ω/ω, where Ω is the steady spin and ω is the disturbance one.

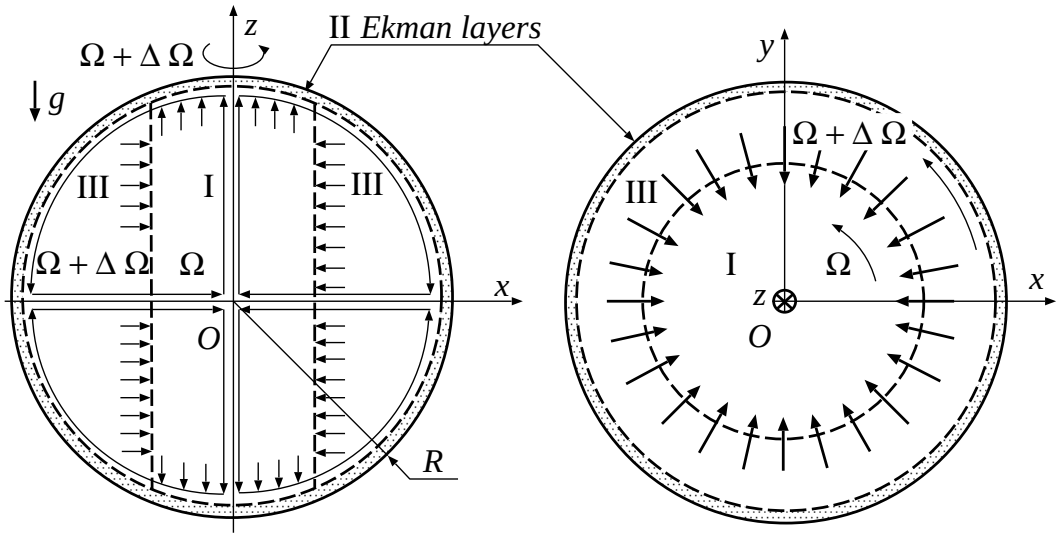

Figure 2: Unsteady low order flow that arising in a closed rotating container when the spin Ω is instantaneously increased with a small amount $\Delta\Omega > 0$: (i) an inwardly moving spin-up front that separates the inner core I at spin Ω and a partly spun-up region III at spin $\Omega + \Delta\Omega$; a thin Ekman boundary layer near the walls (region II) that extract fluid from region I and feed it into the spun-up region III.

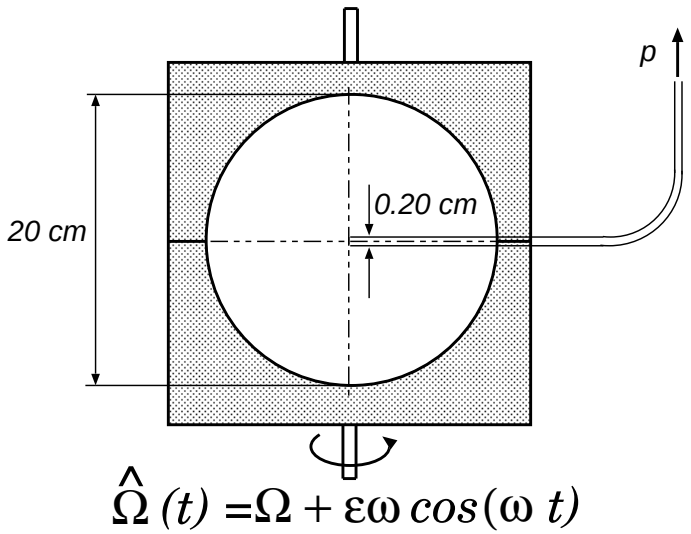

Figure 3: Axisymmetric inertial oscillations of a rotating liquid sphere (Aldridge-Toomre): Fluid container and pressure probe. The container is made of two perspex hemisphere fitted together at the equator, rotated about its vertical spin axis with the nostationary spin $\hat{\Omega}(t) = \Omega + \varepsilon\omega\cos(\omega t)$.

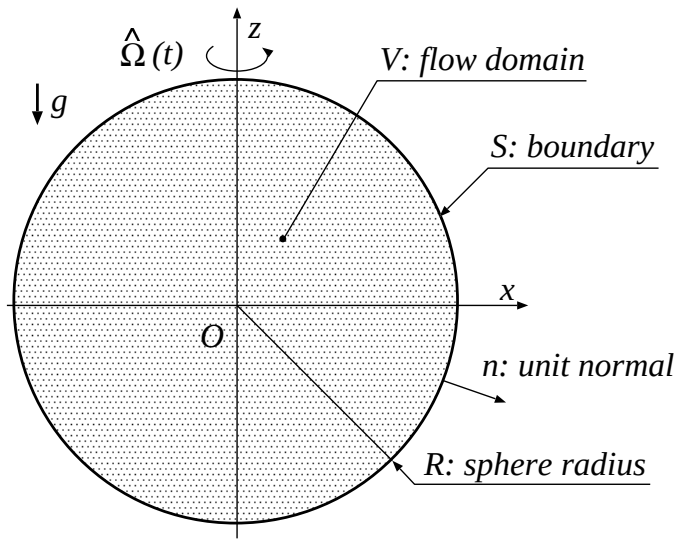

Figure 4: A viscous and incompressible fluid that fill a spherical container which it is rotating with unsteady spin $\hat{\boldsymbol{\Omega}}$ around its vertical axis z. The closed domain flow is V, its surface boundary is S and $\boldsymbol{n}$ is the (exterior) unit normal.

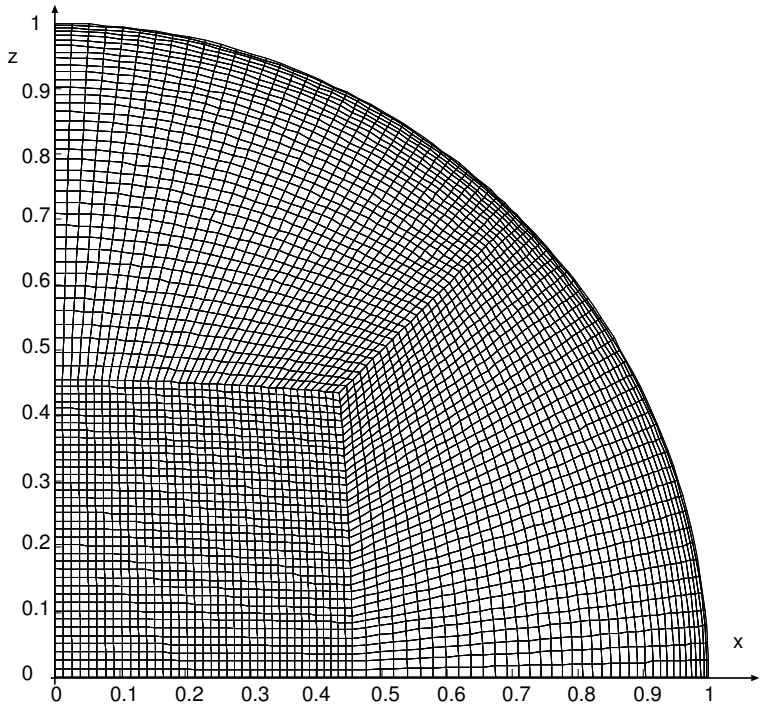

Figure 5: A xz-view (meridional plane) of the finite element mesh used for the numerical simulations of axisymmetric inertial waves.

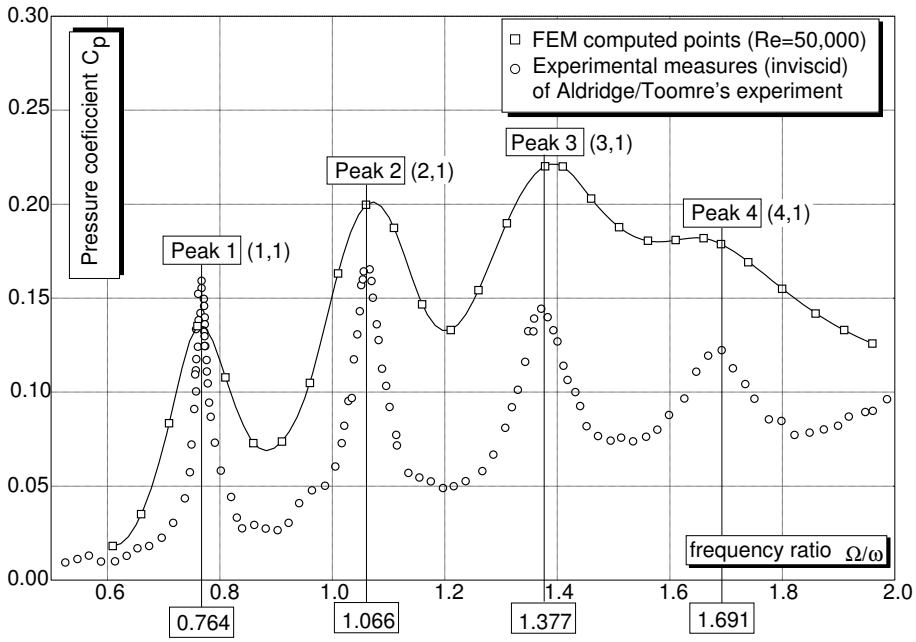

Figure 6: Pressure coefficient C_p at the center of the perturbed rotating unit sphere as a function of the frequency ratio Ω/ω. The sphere is filled with an incompressible viscous fluid. The Reynolds number and kinematic viscosity are 50 000 and 2×10^{-4} $[m^2/s]$, respectively. There are $N_p = 4$ pressure peaks which are identified, which correspond to the axisymmetric (n, m) cell-modes of the inviscid limit $\nu \to 0$ (e.g. see Hide[11], Greenspan[6]).

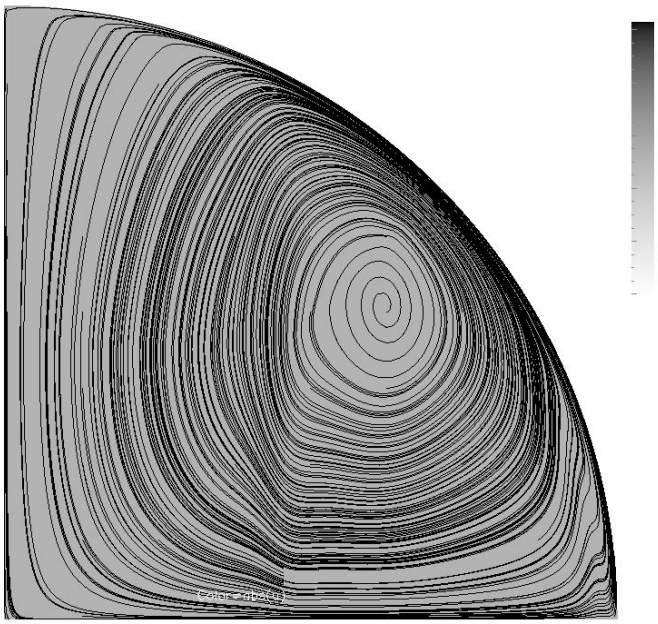

Figure 7: Streamlines in the meridional (vertical) xz upper plane for the perturbed rotating fluid sphere. Pressure-peak 1.

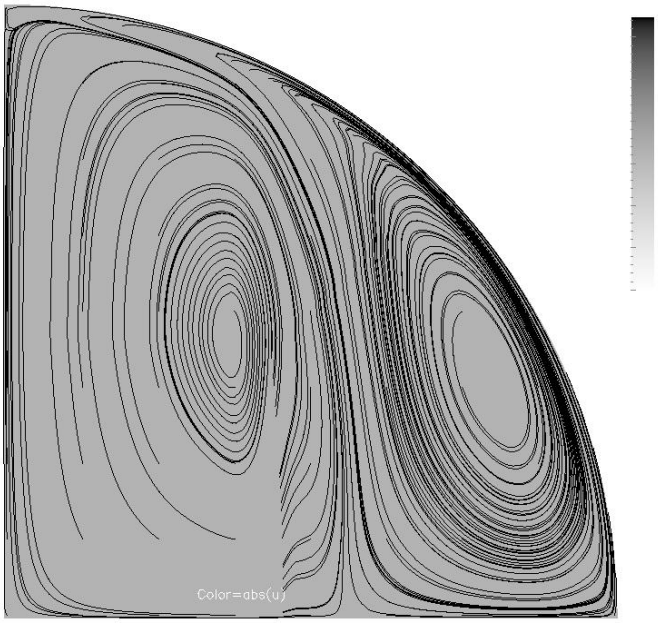

Figure 8: Same as Fig. 7 for pressure-peak 2.

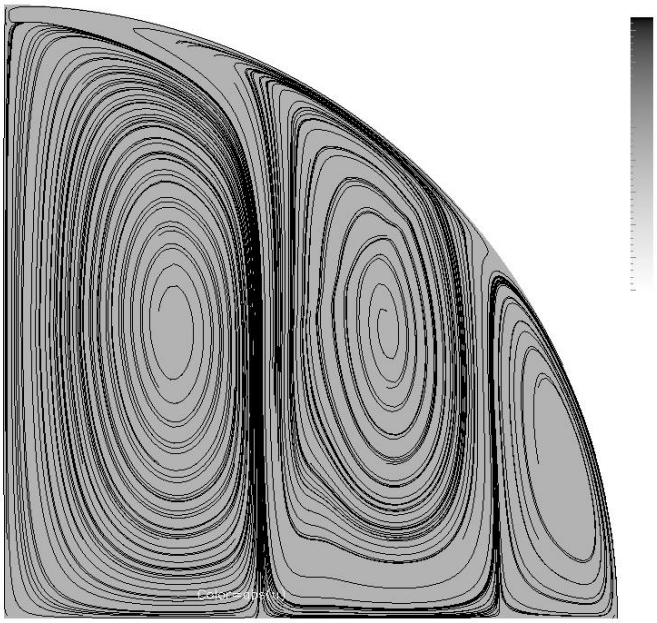

Figure 9: Same as Fig. 7 for pressure-peak 3.

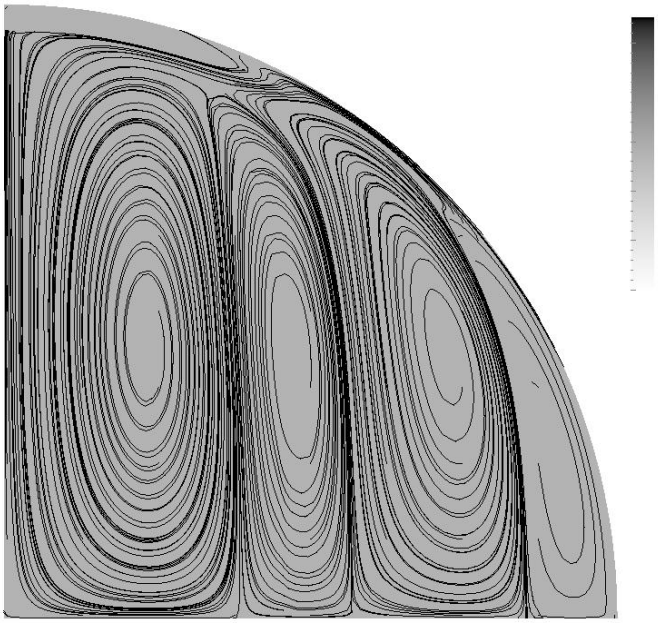

Figure 10: Same as Fig. 7 for pressure-peak 4.

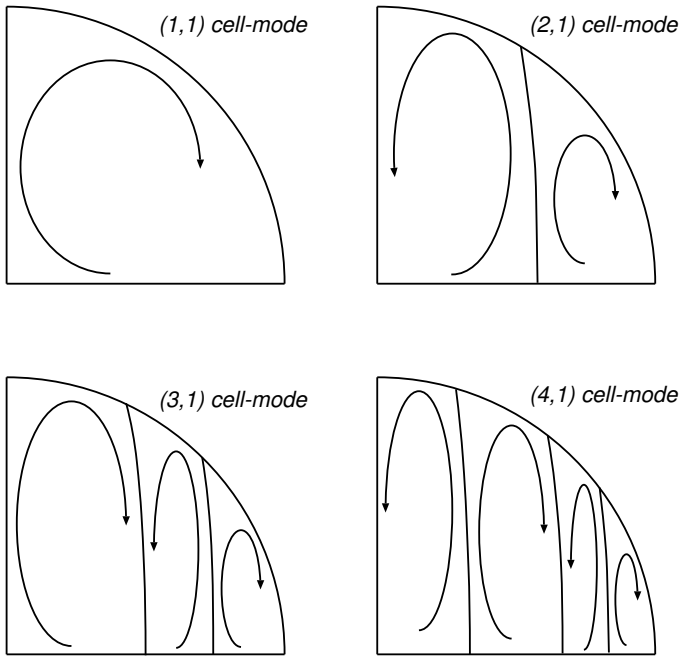

Figure 11: Theoretical circulation patterns corresponding to the first four pressure-peaks predicted by the inviscid theory (e.g. see Hide[11], Greenspan[6]).

List of Tables

similarity number	abbrev.	force ratio	expression
Rossby	Ro	inertia:Coriolis	ω/Ω
Ekman	Ek	viscous:Coriolis	$\nu/(\omega R^2)$
Reynolds	Re	inertia:viscous	$\Omega R^2/\nu$

Table 1: Definition of the non-dimensional similarity numbers: Rossby, Ekman and Reynolds ones.

Ω/ω	Ro	Ek $\times 10^{-5}$
1	1	2
5	0.2	10

Table 2: The Rossby and Ekman numbers corresponding to the frequency-ratio interval $1 \leq \Omega/\omega \leq 5$ when $\Omega = 1$ [rad/s].

(n,m) cell-mode	x_{nm}	$\Omega/\omega_{n,m} = 1/(2x_{nm})$
(1,1)	0.6547	0.76371
(2,1)	0.4688	1.06655
(3,1)	0.3631	1.37703
(4,1)	0.2958	1.69033

Table 3: Adimensional eigenfrequencies $\Omega/\omega_{n,m}$ of the axisymmetric inertial waves in a perturbed rotating unit sphere, where $x_{n,m}$ is the mth of the n zeros of the first associated Legendre polynomial $L_{2n+2,1}(x)$ of $2n+2$ order, in the interval $0 < x < 1$, predicted by the inviscid theory of Stewartson/Roberts[22].

sample	ω	Ω/ω	(n,m) cell-mode (inviscid case)
1	1.30890	0.7640	(1,1)
2	0.93810	1.0660	(2,1)
3	0.72622	1.3770	(3,1)
4	0.59137	1.6910	(4,1)

Table 4: Eigenfrequencies ratio and type of the cell-mode in the inviscid limit $\nu \to 0$ for the first $N_p = 4$ peaks found in the present numerical simulations.